Analysis of nonlinear optical and dynamic gain effects of moderate-power, pulse-position-modulated, erbium-doped fiber amplifiers for deep-space applications

Haomin Yao,[1,*] Malcolm W. Wright,[2] and John R. Marciante[1]

[1]The Institute of Optics, University of Rochester, Rochester, New York 14627, USA

[2]Jet Propulsion Laboratory, California Institute of Technology, Pasadena, California 91109, USA

*Corresponding author: hayao@optics.rochester.edu

Received 5 May 2014; revised 15 August 2014; accepted 18 August 2014;
posted 19 August 2014 (Doc. ID 211413); published 12 September 2014

Lasers for use in deep-space applications such as interplanetary optical communications employ multiwatt resonantly pumped dual-clad erbium-doped fiber amplifiers and the pulse-position modulation scheme. Nonlinear optical effects and dynamic gain effects often impair their performance and limit their operational range. These effects are analyzed theoretically and numerically with a time-dependent two-level propagation model, respectively. Self-phase modulation and stimulated Raman scattering are found to limit the usable data format space. In operational regimes free from nonlinear effects, dynamic gain effects such as the variation in the output pulse energy and square-pulse distortion are quantified. Both are found to primarily depend on the symbol duration and can be as large as 28% and 21%, respectively. © 2014 Optical Society of America

OCIS codes: (060.2320) Fiber optics amplifiers and oscillators; (140.3500) Lasers, erbium; (140.3280) Laser amplifiers; (230.2285) Fiber devices and optical amplifiers; (060.2605) Free-space optical communication.

http://dx.doi.org/10.1364/AO.53.006155

1. Introduction

Free-space optical communication systems for interplanetary ranges require laser transmitters with moderate average power (multiwatt). Many requirements dictate the use of a master-oscillator/power amplifier configuration in which the amplifier can be a resonantly pumped dual-clad erbium-doped fiber amplifier (EDFA) for high efficiency [1]. Due to its simplicity, robustness, and power efficiency, the pulse-position modulation (PPM) format [2] is often baselined for long-range optical communications over interplanetary distances where photon starved optical links are required. In M-ary PPM, every symbol is divided into M slots with a "guard time" for synchronization and to provide a delay at the maximum pulse repetition frequency. For standard PPM, each symbol contains one optical pulse with the information encoded in the position of the pulse among the M possible slots, as illustrated in Fig. 1.

Although the PPM data format has significant advantages in terms of robustness at low signal levels, it requires much higher peak powers from the laser source compared to a simple on–off (binary) data scheme whose average duty cycle is 50%, resulting in peak pulse power that is only twice as large as the average power. Typical projected PPM data schemes for deep-space communications require at least 64-ary or 64 slots, resulting in peak powers that

1559-128X/14/276155-07$15.00/0

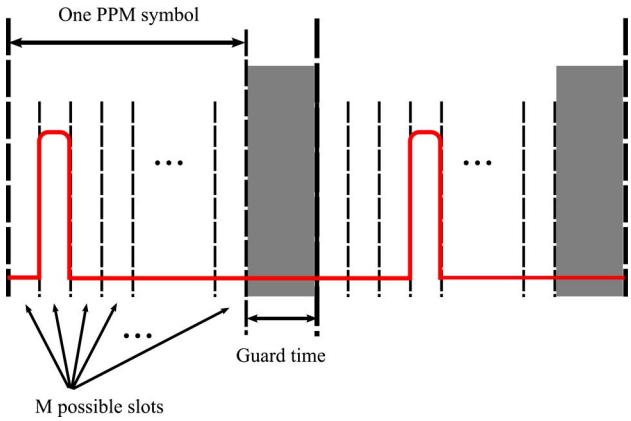

Fig. 1. Schematic of the pulse-position modulation (PPM) format. Plot is not drawn to scale.

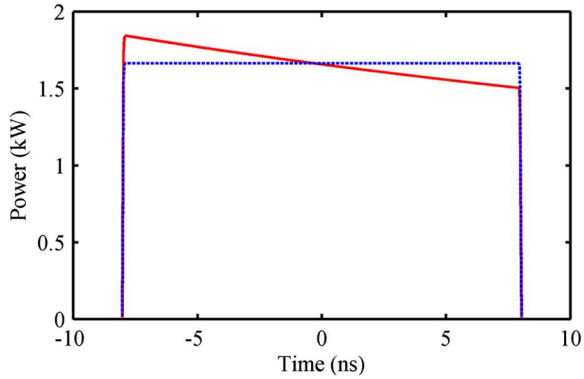

Fig. 3. Distorted output waveform (red solid) of a fiber amplifier overlaid with an undistorted square-shaped input (blue dashed) for comparison under conditions of intrapulse gain saturation.

are more than 60× higher than the average power [3], which can lead to significant nonlinear optical (NLO) impairments.

Gain dynamics may also affect the performance of these fiber amplifiers. PPM symbol rates for deep-space communications (potentially from 200 kHz–300 MHz) result in an interpulse gap as long as a few microseconds. This gap is not negligible compared with the population recovery time of the amplifier under typical pumping conditions. Moreover, this gap varies from pulse to pulse due to the PPM data modulation scheme, so the gain experienced by each pulse varies. Therefore, even for an input train of identical pulses, the energy of the output pulses will fluctuate depending on the pulse pattern, as shown in Fig. 2, resulting in a noise source that can lead to increased bit-error rate, particularly at low photon count. This is drastically different than the case of telecommunications EDFAs where the high (tens of gigahertz) data rates mimic continuous-wave (CW) gain extraction, resulting in no pulse-to-pulse fluctuations.

The gain dynamics can also produce undesirable effects within a single pulse. At these symbol rates, the output pulse energy can reach 26 μJ, which is not negligible compared with the saturation energy of the fiber amplifier $E_{\mathrm{sat}} = Ah\nu/(\sigma^{\mathrm{abs}} + \sigma^{\mathrm{emi}}) \approx 140$ μJ [4]. In this case, intrapulse gain saturation can occur, in which the leading edge of the pulse saturates the gain, leaving less gain for the trailing edge. For square-shaped input pulses, where this effect is most easily observed, the output will therefore not be square shaped. This effect, called square-pulse distortion (SPD) [5], is illustrated in Fig. 3.

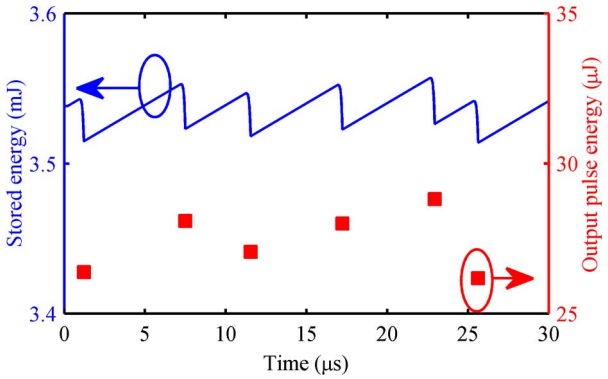

Fig. 2. Stored energy (blue line) in a typical fiber amplifier for a randomly spaced pulse train, and the energy of the output pulses (red squares). A symbol duration of 5 μs was chosen to maximize the effect.

The theory for pulse propagation in a saturable optical amplifier was established by Frantz and Nodvik [6]. Desurvire studied the dynamics of gain saturation and recovery in EDFAs with respect to the pump and signal power using rate equations [7]. SPD was studied in unsaturated EDFAs numerically by Ko *et al.* [8]. Wang and Po performed a detailed analysis of the dynamic characteristics of ytterbium-doped fiber amplifiers at 10–100 kHz pulse repetition (rep) rates and mJ-level pulse energies, showing deep SPD for high-energy pulses [9]. However, the operational regime of the EDFA for the deep-space laser transmitters considered here is different from these previous works. On the one hand, the repetition rate is much lower than that of telecommunication EDFAs, where the variation in output pulse energy is effectively negligible. On the other hand, PPM deep-space systems do not operate in the low-rep-rate regime, such as Ref. [9], in which there is no variation in output pulse energy because the inversion has sufficient time to fully recover to the same state before the next pulse arrives. Therefore, this unique regime requires a systematic study on the dynamic gain effects under a continuum of data formats, which has not been done before to the best of our knowledge.

In this work, an analysis of the NLO effects is first performed to determine the allowable operational data format of an optimized resonantly pumped dual-clad EDFA to be used as part of a laser transmitter for next-generation, deep-space optical communication systems. The dependence of the dynamic gain effects on the data format within the usable data format space is then numerically studied to assess the impact on pulse energy statistics and SPD. Although the specific numerical results use the

architecture optimized in Ref. [1], the trends are applicable to other systems regardless of pumping scheme (resonant or nonresonant [7]) or rare-earth gain dopant (e.g., Er, Yb [9], Tm [10]). The paper is organized as follows: the time-dependent model of the EDFA used in the simulations is explained in Section 2. Sections 3 and 4 are devoted to the analysis of the NLO effects and the dynamic gain effects, respectively. Section 5 provides a brief discussion of the observations and summarizes the results of the paper.

2. Time-Dependent Model of the EDFA

The time-dependent model for the EDFA is developed based on a steady-state model previously developed for CW EDFAs [1]. The rate equations and the light propagation equation are given by

$$\partial N_2^{(s)}/\partial t = \sum_\lambda \Gamma_\lambda^m (P_{\lambda,+} + P_{\lambda,-})(\sigma_\lambda^{\mathrm{abs}} N_1^{(s)} - \sigma_\lambda^{\mathrm{emi}} N_2^{(s)})/A_{\mathrm{Er}} h\nu - N_2^{(s)}/\tau_2 - C N_2^{(s)2}, \quad (1)$$

$$\partial N_2^{(p)}/\partial t = \sum_\lambda \Gamma_\lambda^m (P_{\lambda,+} + P_{\lambda,-}) \times (2\sigma_\lambda^{\mathrm{abs}} N_1^{(p)} - \sigma_\lambda^{\mathrm{emi}} N_2^{(p)})/A_{\mathrm{Er}} h\nu - N_2^{(p)}/\tau_2, \quad (2)$$

$$\frac{1}{v_g}\frac{\partial P_{\lambda,\pm}}{\partial t} \pm \frac{\partial P_{\lambda,\pm}}{\partial z} = [(N_2^{(s)} + N_2^{(p)})\sigma_\lambda^{\mathrm{emi}} - (N_1^{(s)} + 2N_1^{(p)} + N_2^{(p)})\sigma_\lambda^{\mathrm{abs}}]\Gamma_\lambda^g P_{\lambda,\pm} + (N_2^{(s)} + N_2^{(p)})\sigma_\lambda^{\mathrm{emi}}\Gamma_\lambda^g h\nu\Delta\nu - \alpha_\lambda P_{\lambda,\pm} + S \cdot R_\lambda P_{\lambda,\mp}. \quad (3)$$

The Er^{3+} population (N) is divided into single (s) and paired ions (p) according to the model for pair-induced quenching [11]. Each can be in the ground (1) or first excited (2) state. Co- (+) and counterpropagating (−) optical power (P) is spectrally resolved and labeled with the wavelength in the subscript to account for amplified spontaneous emission. The other concentration quenching effect, cooperative upconversion [12], is incorporated through the quadratic term in Eq. (1). The Er^{3+} doping area equals the core area since Er^{3+} is assumed to be uniform across the core. The overlap factors Γ_λ^m and Γ_λ^g are defined such that they capture the spatially dependent gain in large mode-area fiber amplifiers, as described in Ref. [1]. is the wavelength-dependent Rayleigh scattering coefficient and S is the capture fraction of the fiber [13]. The parameters for the dual-clad erbium-doped fiber are taken from the optimized design in Ref. [1], which are listed in Table 1 and Ref. [14]. The average output power, amplification factor, and the effective mode area under this configuration are also listed. It is worth noting that this is a single-mode fiber design, with a minimum bend radius of 5 cm required to avoid bend-induced loss.

Table 1. Parameters of the EDFA

Parameter	Value
Core diameter (μm)	13.4
Numerical aperture	0.09
Effective mode area (μm^2)	170
Doping density, N ($10^{25}/m^3$)	1.4
Fiber length (m)	56
Average seed power, P_{seed} (mW)	200
Average output power (W)	5.6
Amplification factor, G	28
Pump power (W)	10
Power-conversion efficiency	54%

The time-dependent rate- and light-propagation equations were solved with a finite-difference scheme. The fiber was divided into 10,000 segments and the temporal step was related to the spatial step by the group velocity. The CW state was first solved for with the steady-state code, whose results were used as the initial condition for the time-dependent code. The boundary conditions applied were constant pump power, zero forward/backward amplified spontaneous emission at the front/back end, and a predefined seed pulse train.

The CW part of the code was validated in Ref. [1]. Inclusion of the time dependence was validated by calculating the amplification of a single pulse with the same peak power as the CW seed power (200 mW). The snapshots of the pulse propagation in the amplifier are shown in Fig. 4. At every instance, both the power and the shape of the pulse match the power growth curve under CW conditions.

3. Limitations Imposed by Nonlinear Optical Effects

The specifications of the desired transmitter data format are summarized in Table 2. The bandwidth of the receiver filter refers to the available portion of the bandwidth (i.e., not allocated to Doppler shift). As discussed in the introduction, practical values of M leave the peak power in the amplifier ranging from several hundred watts to a few kW. When taken together with the optimum fiber length of a few tens

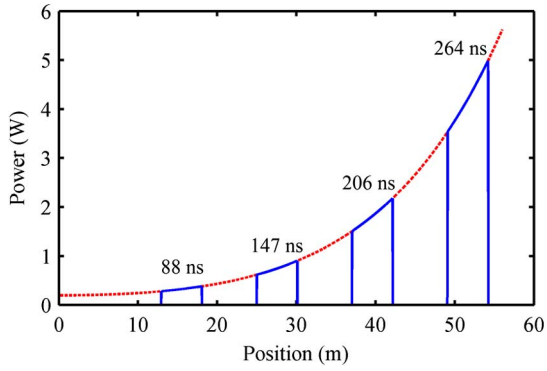

Fig. 4. Snapshots of the amplification of a single pulse with 200 mW peak power at different times from launch. The power and shape of the amplified pulse (blue solid) match well with the power growth curve (red dashed) under CW condition with 200 mW seed.

Table 2. Nominal Specifications of the Transmitter Data Format

Parameter	Value
Symbol repetition rate (MHz)	0.2–300
Number of slots per PPM symbol	≥32
Guard time	1/3 of PPM symbol duration
Pulse shape	Nominally square
Pulse width, τ (ns)	0.2–16
Pulse rise/fall time (ps)	35
Optical bandwidth of the receiver filter (GHz)	5
Average power of seed pulse train (mW)	200

of meters and the effective mode area of ~170 μm^2, this high peak power may result in stimulated Raman scattering (SRS) and self-phase modulation (SPM) that make some of the nominal operational range (repetition rate and pulse width) unsuitable. SBS, a typical limitation in high-power fiber laser systems, is not significant for these systems, as will be discussed below.

Raman scattering is the interaction of light with optical phonons in the medium [15]. In a glass fiber, the scattered light is redshifted from the signal by ~13 THz [16] so that it falls out of the passband of the receiver filter. At sufficiently high optical powers, Raman scattering becomes a stimulated process in which a large portion of the signal power is scattered and becomes unusable. In the pulsed regime, the copropagating Stokes pulse will nominally walk off the signal pulse due to group velocity dispersion. However, for the short length of fiber in our case, the walk-off can be neglected. Therefore, the SRS threshold for CW light [17] can be approximately used:

$$\frac{g_R \int_0^L P(z)\mathrm{d}z}{A_{\mathrm{eff}}} \approx 16. \tag{4}$$

The integral is calculated using the power growth along the fiber obtained from Ref. [1]:

$$\int_0^L P(z)\mathrm{d}z = \eta P(L)L = \eta G P(0)L = \eta G \frac{T}{\tau} P_{\mathrm{seed}} L. \tag{5}$$

In this equation, the factor η represents the averaging of the power growth along the fiber. In this sense, it serves to provide an effective average power along the fiber. Its value for the case under study is calculated to be ~0.254. The resulting SRS threshold is

$$\frac{T}{\tau} \approx 580, \tag{6}$$

in which T is the sum of one PPM symbol duration and the guard time.

SPM is the nonlinear phase shift due to propagation in a medium with third-order NLO susceptibility [15]. For a pulsed signal, SPM broadens its bandwidth, which leads to power loss when the signal bandwidth exceeds the filter bandwidth at the receiver. The output spectrum was calculated by Fourier transforming the output waveform with a nonlinear phase shift in the form of [15]:

$$E_{\mathrm{out}}(L,t) \propto \sqrt{P(L,t)}\exp(i\phi_{\mathrm{NL}}) \approx \sqrt{G\cdot P(0,t)}\exp\left[in_2\frac{\eta G\cdot P(0,t)}{A_{\mathrm{eff}}}\frac{2\pi}{\lambda_s}L\right]. \tag{7}$$

By using the input waveform multiplied by the amplification factor, SPD is neglected. This is justified by noting that the SPM contribution primarily comes from the sharp rising and falling edges rather than from the slowly varying pulse top. The bandwidth that contains 86% of the total power was calculated from the output spectrum and is plotted as a function of the pulse width and the sum of the PPM symbol duration and guard time in Fig. 5. The slanted line indicates the limit on the data formats from the 32-ary PPM format; other M-ary PPM formats can be obtained by shifting this line to the right in the figure. As would be expected, the SPM-induced bandwidth broadening is negligible for longer pulses, because the pulse edges where the SPM contribution mainly comes from only account for a small portion of the whole waveform. The effect of SPM increases with decreasing pulse width and becomes most significant for short pulses with a long symbol duration, because the peak power is the highest. The slight "stair-case" structure observed in the 1–100 GHz lines also comes from the finite pulse edges. For square-shaped pulses with realistic rise and fall times, the SPM effect does not result in continuous broadening of the optical spectrum but rather splits off spectral sidelobes, as illustrated in Fig. 4.4 in Ref. [18]. With increasing propagation distance (equivalent to increasing peak power in the present work), these sidelobes move away from the central peak and decrease in intensity. As a result, the boundary for the 86% fraction expands relatively fast with increasing peak power when it stays on one pair of

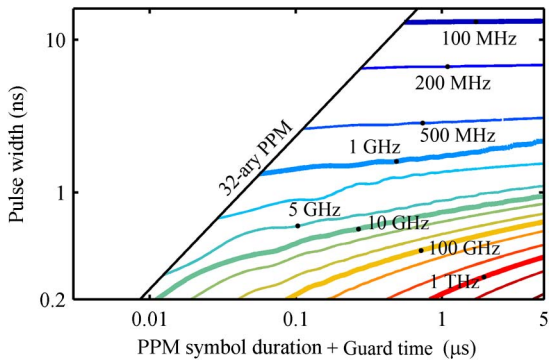

Fig. 5. SPM-induced optical bandwidth of the output signal as a function of pulse width and the sum of symbol duration and guard time.

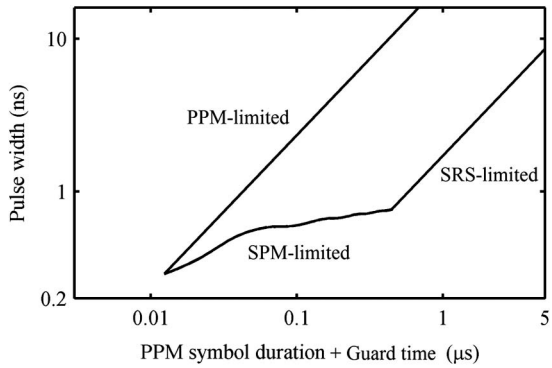

Fig. 6. Usable data format space of the laser transmitter with constraints imposed by nonlinear effects.

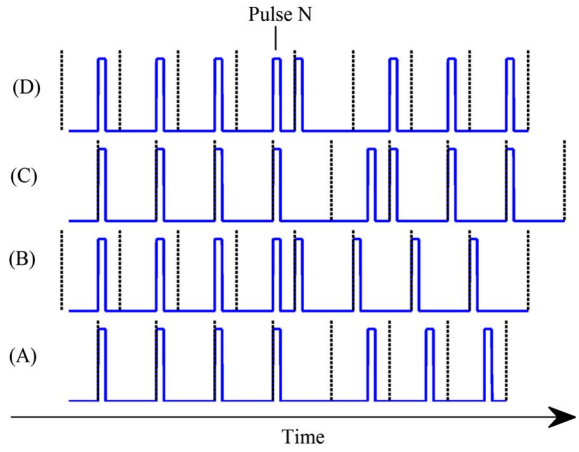

Fig. 7. Input pulse trains designed to simulate the maximum variation in the energy and SPD of the output pulses. Four cases of interest are (from bottom up): (A) a pulse with the maximum preceding gap; (B) a pulse with the minimum preceding gap; (C) a pulse with the maximum preceding gap immediately followed by one with the minimum gap; and (D) a pulse with the minimum preceding gap immediately followed by one with the maximum gap. The PPM symbol slots are indicated by the dashed lines. Plots are illustrative and not drawn to scale.

sidelobes but relatively slowly when it "jumps" from one pair of sidelobes to the next pair inside them.

While Fig. 5 represents the complete impact of SPM, the goal was to define an operational regime for use in the PPM data transmitter. As such, the contour line at 5 GHz was selected as the lower-limit boundary for data format due to the bandwidth of the filter at the receiver.

Stimulated Brillouin scattering (SBS) is the interaction of light with acoustic phonons in the medium [15]. While SBS is typically a significant problem in high-power narrow-linewidth fiber amplifiers, it can be suppressed in practice by techniques such as phase modulation to broaden the optical bandwidth outside the SBS bandwidth. Since the bandwidth of the receiver filter in a deep-space optical communication system is significantly larger than the SBS bandwidth, SBS can be neglected in the context of deep-space laser transmitters.

Combining the limitations imposed by NLO effects, the allowable operational regime that avoids these limitations is shown in Fig. 6. This regime is defined on the bottom by SPM-induced bandwidth, on the right by SRS, and on the left by the nature of the PPM data format, that the duty cycle is set by the guard time and the number of slots per symbol. Note that the nominal operational regime, represented by the area of the plot to the right of the PPM limit, has been reduced to about 45% of its original size by NLO effects in the fiber amplifier.

4. Dynamic Effects in the Pulsed Amplifier

Even for data formats within the usable regime defined by Fig. 6, temporal effects arising from the gain dynamics may also impair the performance of the space communication system. To understand the impact of gain dynamics on the output pulses, it is necessary to employ PPM data schemes. While full-scale statistics could be obtained by using a pseudorandom symbol stream, the low symbol repetition rates (long computation time) and large simulation regime (defined by Fig. 6) make such an approach computationally prohibitive. However, since the dynamic effects are primarily driven by the time between consecutive pulses, it is sufficient to define pulse trains that maximize the effects of this spacing. In this way, the maximum impact of gain dynamics can be calculated without obtaining the complete set of statistics.

To this end, four special pulse trains were employed as illustrated in Fig. 7. In the first pulse train (A), Pulse N and all preceding pulses are in the first slot of the PPM symbol. Pulse $N+1$ is placed in the last slot of its symbol, giving it the largest possible separation from Pulse N. Pulse $N+1$ thus experiences the maximum gain. The second pulse train (B) is an exact opposite case, where Pulse N and all preceding pulses are in the last slot, and Pulse $N+1$ is in the first slot. In this case, Pulse $N+1$ experiences the minimum gain. In the third pulse train (C), Pulse N and all preceding pulses are in the first slot, Pulse $N+1$ in the last slot, and Pulse $N+2$ is again in the first. In this arrangement, Pulse $N+1$ experiences the maximum gain while Pulse $N+2$ experiences the maximum drop in gain from that of Pulse $N+1$. Finally, in the case opposite to (C), the fourth pulse train (D) has Pulse N and all preceding pulses in the last slot, Pulse $N+1$ in the first slot, and Pulse $N+2$ again in the last. This allows Pulse $N+1$ to experience the minimum gain and Pulse $N+2$ to experience the maximum increase in gain from that of Pulse $N+1$. For all cases, the initial delay is set to be half of the sum of one symbol duration and guard time, ensuring that the gain for pulses up to Pulse N equals the CW value. These four input pulse trains were run over a 2D grid spanning the operational regime defined by Fig. 6.

In the data analysis of the pulse trains exiting the fiber amplifier, the difference between the maximum and the minimum output pulse energies relative to the mean output pulse energy (taken to be the energy of Pulse N) was recorded as the *peak-to-peak spread*

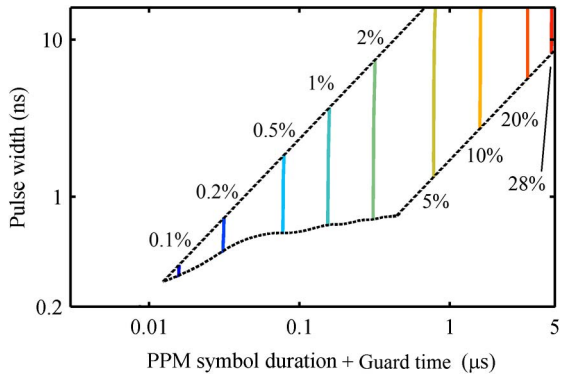

Fig. 8. Peak-to-peak spread of output pulse energy relative to the mean output pulse energy as a function of pulse width and the sum of one PPM symbol duration and guard time.

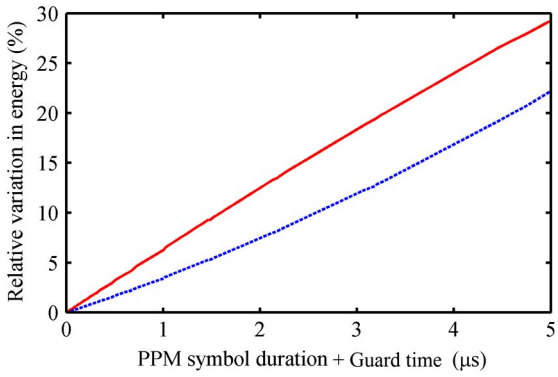

Fig. 10. Relative peak-to-peak spread of output pulse energy (red solid) and maximum energy variation between consecutive pulses (blue dashed) as a function of the sum of one PPM symbol duration and guard time.

of the energy of the output pulses. The larger percentage change of the maximum drop and the maximum increase in output pulse energy between neighboring pulses was recorded as the maximum variation in the output energy *between consecutive pulses*. These quantities are plotted in Figs. 8 and 9. Both the energy spread and the maximum variation between pulses depend on the symbol duration, but not appreciably on the pulse width since the variation in gain depends on the gap between pulses, which in turn depends on the data rate but not the pulse width. Their dependence on the data rate, whose reciprocal is the sum of one symbol duration and guard time, is further illustrated in Fig. 10, with both quantities showing an almost linear trend. The longest and the shortest gaps between pulses are proportional to the symbol duration, which is small compared to the population recovery time (175 μs for the amplifier configuration). Hence the recovery of the stored energy is almost linear in time, as shown in Fig. 2, leading to the observed quasi-linear dependence shown in Fig. 10. The largest value of the peak-to-peak spread and the maximum variation between consecutive pulses is 28% and 21%, respectively.

Due to diffraction and minimization of the required laser transmitter power, the signal power will, in general, be at the photon-counting level by the time it reaches the receiver, and will therefore be driven by Poisson statistics. The variation in the energy of output pulses leads to a fluctuation of mean photon numbers, which may affect signal recovery. Assuming a transmitter aperture diameter of 30.5 cm, a receiver aperture of 3–5 m [3], and a maximum distance between Mars and Earth of 4.013×10^{11} m [19], the mean photon number at the receiver was calculated to be from 0.3 to 500 for the data format used. The probability of detecting any photon (i.e., not a zero) at the receiver is given by

$$P(n \neq 0) = 1 - \langle n \rangle^0 \frac{\exp(-\langle n \rangle)}{0!} = 1 - \exp(-\langle n \rangle), \quad (8)$$

without the benefits of error correction coding. To estimate how the energy fluctuation might impact errors in communications, the variation in this probability was calculated using the data for the fluctuation of output pulse energy in Fig. 8. Its maximum value of 2×10^{-4}, achieved at the shortest symbol duration (8.5 ps), is much smaller than required when error correction codes are utilized [20].

Intrapulse gain dynamics, caused by saturation of the gain within a single pulse, lead to a change in the pulse shape since the leading edge of the pulse experiences more gain than the trailing edge. This effect is most easily quantified by the SPD, which is defined as the percentage drop in gain from the beginning to the end of a square input pulse (essentially the same as that of Ref. [5]). The results from all four pulse trains reveal that the SPD of an output pulse positively correlates with its output energy, in agreement with theory [6]. Therefore, only pulse train (A) was employed to get the maximum SPD (recorded on Pulse $N + 1$), and the SPDs of Pulse N in pulse trains (A) and (B) were averaged to get the mean SPD. The maximum SPD is plotted as a function of the pulse width and the sum of one symbol duration and guard time in Fig. 11. The mean SPD (not shown) has the same dependence on both parameters as the maximum SPD. Its value is also quite close to but less

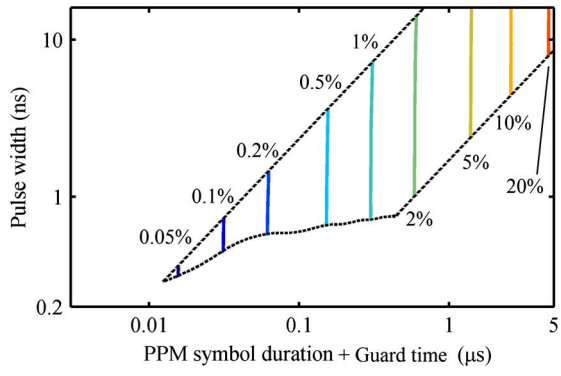

Fig. 9. Maximum variation in the output energy between consecutive pulses relative to the mean output pulse energy as a function of pulse width and the sum of one PPM symbol duration and guard time.

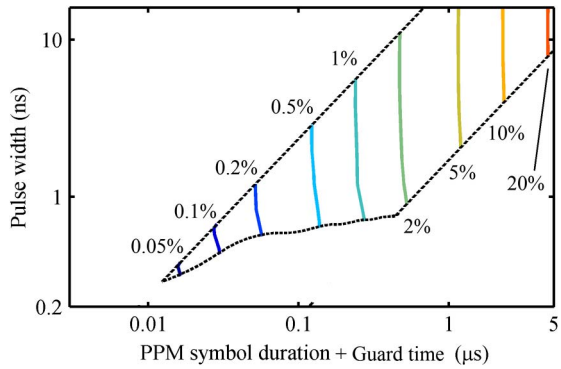

Fig. 11. Maximum SPD as a function of pulse width and the sum of one PPM symbol duration and guard time.

than the maximum SPD throughout the parameter space, with the largest value smaller by a factor of 0.89. Both SPDs primarily depend on the sum of one symbol duration and guard time, in accordance with the theory [6], because the input pulse energy and this sum differ only by a factor of the average seed power. The contour lines shown in Fig. 11 progressively deviate from vertical from the top right corner toward the lower left corner. This seeming violation of the dependence on the data rate comes from the subtlety in calculating SPD with Eq. (27) in Ref. [6]. In this study, SPD was taken between the starting and the ending times between which the pulse's instantaneous power exceeded 98% of its peak power. For pulses as short as 200 ps, the integral in Eq. (27) between these two time instances is non-negligibly less than the total pulse energy because the two 35 ps pulse edges carry a reasonable fraction of the energy. The SPD calculated this way depends on both the data rate and the pulse width. This issue on the calculation becomes less significant for longer pulse widths, as can be seen in the upper part of Fig. 11. Extrapolation of the SPD to that of the whole pulse was performed and the resulting contour lines (not shown) became straight vertical lines. The largest value of the maximum SPD is 21%.

5. Discussion and Conclusions

In summary, the impact of NLO effects and gain dynamics has been analyzed theoretically and numerically in moderate-power EDFAs using PPM data formats suitable for deep-space applications. The operational regime in the PPM-data-format space that is free from NLO effects was identified via theoretical analysis. SPM and SRS were found to limit the usable data formats, reducing the operational regime of the laser transmitter by ~55%. Within this operational regime, dynamic gain effects were numerically studied, and characteristics such as the variation in the output pulse energy and the SPD were mapped on the data format space. Both were found to primarily depend on the symbol duration, with a maximum peak-peak fluctuation in pulse energy of 28% and a maximum SPD of 21%. The implications for photon-counting receivers were also discussed. Finally, the observed trends are applicable to other laser systems regardless of pumping scheme or rare-earth gain dopant.

H. Yao and J. R. Marciante were supported in part by NASA/JPL under Subcontract No. 1440052. The work of M. W. Wright was carried out at the Jet Propulsion Laboratory, California Institute of Technology under contract with the National Aeronautics and Space Administration. H. Yao thanks Jordan Leidner and Dr. George Gehring for helpful technical discussions.

References

1. H. M. Yao, M. W. Wright, and J. R. Marciante, "Optimization of resonantly cladding-pumped erbium-doped fiber amplifiers for space-borne applications," Appl. Opt. **52**, 3923–3930 (2013).
2. J. R. Pierce, "Optical channels: practical limits with photon counting," IEEE Trans. Commun. **26**, 1819–1821 (1978).
3. D. M. Boroson, A. Biswas, and B. L. Edwards, "MLCD: overview of NASA's Mars laser communications demonstration system," Proc. SPIE **5338**, 16–28 (2004).
4. O. Svelto and D. C. Hanna, *Principles of Lasers* (Plenum, 1998).
5. J. K. Lawson, D. R. Speck, C. Bibeau, S. C. Burkhart, M. A. Henesian, C. W. Laumann, T. L. Weiland, and R. B. Wilcox, "Temporal shaping of third-harmonic pulses on the Nova laser system," Appl. Opt. **31**, 5061–5068 (1992).
6. L. M. Frantz and J. S. Nodvik, "Theory of pulse propagation in a laser amplifier," J. Appl. Phys. **34**, 2346–2349 (1963).
7. E. Desurvire, "Analysis of transient gain saturation and recovery in erbium-doped fiber amplifiers," IEEE Photon. Technol. Lett. **1**, 196–199 (1989).
8. K. Y. Ko, M. S. Demokan, and H. Y. Tam, "Transient analysis of erbium-doped fiber amplifiers," IEEE Photon. Technol. Lett. **6**, 1436–1438 (1994).
9. Y. Wang and H. Po, "Dynamic characteristics of double-clad fiber amplifiers for high-power pulse amplification," J. Lightwave Technol. **21**, 2262–2270 (2003).
10. J. Kim, S. S. H. Yam, M. E. Marhic, and L. G. Kazovsky, "Modeling gain dynamics of thulium-doped fiber amplifiers," IEEE Photon. Technol. Lett. **17**, 998–1000 (2005).
11. E. Delevaque, T. Georges, M. Monerie, P. Lamouler, and J. F. Bayon, "Modeling of pair-induced quenching in erbium-doped silicate fibers," IEEE Photon. Technol. Lett. **5**, 73–75 (1993).
12. P. Blixt, J. Nilsson, T. Carlnas, and B. Jaskorzynska, "Concentration-dependent upconversion in Er^{3+}-doped fiber amplifiers: experiments and modeling," IEEE Photon. Technol. Lett. **3**, 996–998 (1991).
13. M. N. Zervas and R. I. Laming, "Rayleigh-scattering effect on the gain efficiency and noise of erbium-doped fiber amplifiers," IEEE J. Quantum Electron. **31**, 468–471 (1995).
14. nLIGHT, "LIEKKI Er60-xx-xxx Datasheet," http://www.nlight.net/nlight-files/file/datasheets/Fibers/nLIGHT_LIEKKI_Er60-xx-xxx_051512.pdf.
15. R. W. Boyd, *Nonlinear Optics* (Academic, 2008).
16. R. H. Stolen and E. P. Ippen, "Raman gain in glass optical waveguides," Appl. Phys. Lett. **22**, 276–278 (1973).
17. R. G. Smith, "Optical power handling capacity of low loss optical fibers as determined by stimulated Raman and Brillouin-scattering," Appl. Opt. **11**, 2489–2494 (1972).
18. G. P. Agrawal, *Nonlinear Fiber Optics* (Academic, 2013).
19. D. R. Williams, "Mars fact sheet," http://nssdc.gsfc.nasa.gov/planetary/factsheet/marsfact.html.
20. B. Moision and J. Hamkins, "Coded modulation for the deep-space optical channel: serially concatenated pulse-position modulation," Interplanetary Network Progress Report 42-161 (2005).